Article

Demonstration of Phase Change Thermal Energy Storage in Zinc Oxide Microencapsulated Sodium Nitrate

Ciprian Neagoe [1],*, Ioan Albert Tudor [1], Cristina Florentina Ciobota [1], Cristian Bogdanescu [1], Paul Stanciu [1], Nicoleta Zărnescu-Ivan [1], Radu Robert Piticescu [1],* and Maria Dolores Romero-Sanchez [1,2]

[1] National R&D Institute for Nonferrous and Rare Metals–IMNR, 077145 Pantelimon, Romania; atudor@imnr.ro (I.A.T.); crusti@imnr.ro (C.F.C.); cbogdanescu@imnr.ro (C.B.); pstanciu@imnr.ro (P.S.); nicoleta.zarnescu@imnr.ro (N.Z.-I.); md.romero@applynano.com (M.D.R.-S.)

[2] Applynano Solutions, S.L., Parque Científico de Alicante, 03690 Alicante, Spain

* Correspondence: ciprian.neagoe@imnr.ro (C.N.); rpiticescu@imnr.ro (R.R.P.)

Featured Application: Microencapsulation of alkali metal nitrates for latent heat storage in concentrated solar power plants has the potential to reduce salt corrosion in storage tanks and installations.

Abstract: Microencapsulation of sodium nitrate ($NaNO_3$) as phase change material for high temperature thermal energy storage aims to reduce costs related to metal corrosion in storage tanks. The goal of this work was to test in a prototype thermal energy storage tank (16.7 L internal volume) the thermal properties of $NaNO_3$ microencapsulated in zinc oxide shells, and estimate the potential of $NaNO_3$–ZnO microcapsules for thermal storage applications. A fast and scalable microencapsulation procedure was developed, a flow calorimetry method was adapted, and a template document created to perform tank thermal transfer simulation by the finite element method (FEM) was set in Microsoft Excel. Differential scanning calorimetry (DSC) and transient plane source (TPS) methods were used to measure, in small samples, the temperature dependency of melting/solidification heat, specific heat, and thermal conductivity of the $NaNO_3$–ZnO microcapsules. Scanning electron microscopy (SEM) and chemical analysis demonstrated the stability of microcapsules over multiple tank charge–discharge cycles. The energy stored as latent heat is available for a temperature interval from 303 to 285 °C, corresponding to onset–offset for $NaNO_3$ solidification. Charge–self-discharge experiments on the pilot tank showed that the amount of thermal energy stored in this interval largely corresponds to the $NaNO_3$ content of the microcapsules; the high temperature energy density of microcapsules is estimated in the range from 145 to 179 MJ/m^3. Comparison between real tank experiments and FEM simulations demonstrated that DSC and TPS laboratory measurements on microcapsule thermal properties may reliably be used to design applications for thermal energy storage.

Keywords: phase change materials; sodium nitrate; thermal conductivity; microencapsulation; latent heat; thermal energy storage

1. Introduction

Thermal energy storage is important for the development of industrial and domestic applications that optimize energy production and use. Efficiency of thermal energy storage systems depends, among other factors, on the properties of the storage material to accumulate and release energy by either changing its temperature, in sensitive heat storage, or undergoing a phase transition, in latent heat storage (for a review, see Sarbu and Sebarchievici, 2018) [1]. Storing energy as latent heat may provide a large amount of energy at almost constant temperature, an important feature in some technical applications that require close control over temperature, and may be a robust and inexpensive alternative to temperature control automation by electronic devices.

Selection of a material suitable for latent heat energy storage (see Podara et al., 2021) [2] considers multiple criteria such as temperature for phase change, latent heat, thermal

stability of the material, containment, and cost (Hussam et al., 2020) [3]. Sodium and potassium nitrate salts as phase change materials (PCM) cover the range of relatively high temperatures of interest (300–400 °C) for concentrated solar plants (CSP). Sodium nitrate undergoes a solid–liquid phase change transition at 307 °C (Xu et al., 2018) [4], whereas potassium nitrate melts at higher temperature, 336 °C (Mohammad 2017; D'Aguanno et al., 2018) [5,6]. The latent heats of solid–liquid transition in sodium and potassium nitrate salts are 5.9 and 11.8 times, respectively, smaller than the latent heat for LiF solidification (1.04 MJ/kg at 849 °C). The tradeoff between energy storage capacity and the melting temperature of the material may consider that (a) higher or lower temperatures may not be technically suited for a specific application, (b) temperature increase is associated with accelerated corrosion of containers and pipes, and (c) the heat loss rate from the storage container depends directly on the temperature gradient across the container shell.

For sodium nitrate PCM, limitations of tank charge–discharge rates are related to the low thermal conductivity of the storage material (Bellan et al., 2015) [7]. Micro and macroencapsulation may increase the thermal conductivity of the storage material if a highly conductive shell material is used (Huang et al., 2019; Cáceres et al., 2017) [8,9]. Similarly, composite materials are explored, where a matrix of chemically stable, thermally conductive material mitigates the problem of a highly corrosive and low conductive inorganic salt (or salt mixture) used to store the thermal energy (Courbon et al., 2020; Podara et al., 2021) [2,10].

The thermal properties of the storage material may be combined with appropriate design of the storage tank using in silico experiments of computational fluid dynamics (CFD) (Al-abidi et al., 2013) [11]. The finite element method (FEM) with common software packages (Comsol Multiphysics) was used to compare various inorganic salt PCMs and different suitable PCM-encapsulation materials to render economically viable solutions that would meet the requirements of thermal energy storage (TES) for CSP (Cáceres et al., 2017) [9].

Micro and nanoencapsulation has been frequently reported for low temperature regime PCMs, mainly using organic polymers as shell materials. For high temperature applications (e.g., CSP), manufacturing micrometer-scale shells that are stable over many PCM melting–solidification cycles is challenging for at least two reasons: (a) coatings made by the versatile organic polymer technology do not withstand high temperatures; and (b) water-based chemistry to prepare shells may dissolve the PCM core, which is typically an inorganic salt/salt mixture [12]. SiO_2 coating of micrometer-size alkaline nitrate cores was recently demonstrated by several groups (Zhang et al., 2018; Romero-Sanchez et al., 2018; Lee and Jo, 2020) [12–14]. A method for microencapsulation of nitrate salts in zinc oxide shells was developed within a project funded by the National Authority for Scientific Research in Romania (project acronym ENERHIGH), as described in our previous papers (Romero-Sanchez et al., 2019; Tudor et al., 2018) [15,16]. Briefly, in that work, KNO_3–ZnO microcapsules were prepared from raw materials (zinc nitrate tetrahydrate and potassium nitrate) by the solvothermal method. Spherical morphology of the ZnO-covered KNO_3 microparticles was observed after spray drying, with particle sizes of only a few microns.

The aim of this work is to evaluate the capacity of $NaNO_3$–ZnO microcapsules to store thermal energy and the possibility to retrieve it at high temperatures. To improve the scalability of microcapsule fabrication, a novel protocol for microencapsulation was elaborated and tested, consisting in direct ZnO coating of $NaNO_3$ particles using commercially available $NaNO_3$ grains (relatively large, up to 0.5 mm size) and ZnO powder (0.1 to 2 μm particles) as raw materials. Up to 22.1 kg of $NaNO_3$–ZnO microcapsules were thus prepared. Results from experiments in a 16.7 L cylinder-shaped prototype tank are presented, which show that microcapsules store significant amounts of thermal energy in solid–liquid $NaNO_3$ transitions. To facilitate further development of novel PCM materials for energy storage, a platform for combined in silico prototype-scale investigation was built. For a simplified tank FEM model, thermal transfer is presented in simulations of tank discharge and compared with real temperature data from prototype tank experiments

on microcapsules. The goal is to understand and predict material performance in thermal storage applications, starting from material characterization by laboratory methods.

2. Materials and Methods

Chemicals. Analytical grade reagents were used in all experiments. Sodium nitrate was purchased from Roth, Germany. Zinc oxide was provided by Chimreactiv, Romania.

Microcapsules. $NaNO_3$ was encapsulated in ZnO shells at 4:1 mass ratio, using a simplified protocol derived from our previous work (Tudor et al., 2018) [16]. Basically, commercially available $NaNO_3$ powder grains, ZnO, and ethanol were mixed and stirred to achieve homogenous dispersion of components. The mixture was then subjected to a thermal treatment for 1 h at 200 °C in atmospheric air. Microcapsules were characterized by scanning electron microscopy and energy dispersive X-ray spectroscopy to determine their structure and demonstrate encapsulation.

Chemical analysis of the thermal energy storage material was determined by flame atomic absorption spectrometry (ISO 11047:1999) for Na and Zn and wet chemistry (ISO 5664: 2001) for NO_3^-. Samples were taken from the tank at 14 different positions in the storage material.

Scanning Electron Microscopy (SEM) and Energy Dispersive X-ray Spectroscopy (EDS) were performed on microcapsules using an SEM–EDS Quanta 250 scanning electron microscope (FEI Company, Eindhoven, The Netherlands) equipped with the Element Silicon Drift Detector Fixed and Element EDS Analysis Software Suite APEX™ 1.0, EDAX, Mahwah, NJ, USA. Thus, by EDS, the atomic composition of a selected spot was determined. In the report from the instrument, the abbreviations C K, O K, ZnL, NK, NaK, and AlK are used to indicate that the data are based on detection of energies for specific orbital transitions, corresponding to elements: C, O, Zn, N, Na, and Al, respectively. The elemental composition of each spot is reported as relative weight (%), atom concentration (%), or the net intensity (a.u.) of the respective element-specific peak. For microcapsules, the carbon % reported in analysis is background from the sample immobilization device, and was subtracted from further calculations.

Thermal analysis. Thermal conductivity and thermal diffusivity/specific volumetric heat determinations were made by the transient plane source method (TPS-2200 from Hot Disk, Sweden, model 5082 mica sensor). In laboratory determinations, microcapsule powder was poured to fill a 200 mL stainless steel beaker, the sensor was embedded in the middle, the assembly was placed in the empty (air-filled) storage tank, then exposed to multiple temperature cycles in the 25 to 350 °C temperature interval. The thermal conductivity and specific volumetric heat curves were recorded only after the second cycle of microcapsule melting–solidification, when the microcapsule material was a compact porous material block; thus, the thermal parameters are representative for the material formed after multiple energy storage cycles. Temperature monitoring was achieved by tank thermocouples and corrected to report in-place temperatures using calibrated readings for the sensor resistivity.

Differential Scanning Calorimetry (DSC) was performed using two instruments: SET-SYS Evolution from Setaram and DSC F3 Maia from Netzsch, Germany. Microgram amounts of $NaNO_3$ and microcapsules were heated–cooled in cycles to determine melting and crystallization temperatures and enthalpies.

Prototype tank. The thermal storage tank is a right circular cylinder (referred to as the tank cylinder), 0.55 m length, 0.2 m diameter, made of 2 mm-thick stainless steel (SS 316), accommodating temperature sensors in inbuilt sheaths protruding transversally up to the longitudinal axis. A thermal conductivity sensor is located in a holder at the center-bottom of the tank. The cylinder is wrapped in 0.2 m thick Ravaber mineral foam insulation. A stainless-steel envelope covers the insulation to a final cylinder length of 0.95 m and diameter of 0.6 m. Material loading gates (three 20 mm diameter holes) are placed at the top of the storage tank and accessible from outside by cap closed tubes that span the thermal insulation. The heat exchanger is made of a SS 316 tube (12 mm outer diameter, 10 mm

inner diameter, 5.04 m length), shaped as a helical-coil wrapped around the longitudinal axis in 15 loops (120 mm diameter). Mineral oil is used as a heat transfer fluid (HTF) at a temperature that is maintained by an external recirculating pump with heating/cooling capability. Temperatures were continuously monitored (digital recording) by eight type J thermocouples (T1–T8) placed as indicated in Figure 1. For the 50 to 400 °C measurement interval, the thermocouples were linearly calibrated to work within a ±1.5 °C reading error. T3, T4, and T5 measured temperatures inside the tank, at the central longitudinal axis, and they protruded to their measurement spot through tank-fixed one-end-closed tubular sheets (5 mm outer diameter, 3 mm inner diameter, 0.5 m long). The relative positions of the protruding thermocouple sheets and heating coil loops were designed to maximize the separation space and avoid contact. Temperatures were monitored across the energy storage material for two sections that are transversal to the tank cylinder, by placing T1 and T2 directly on the outer surface of the tank cylinder, at the same longitudinal positions as their corresponding T4–T3 (respectively) pair. T7 and T8 were in direct contact with the heating coil at the tank-envelope entry and exit points. The installation is pictured in a previous publication (Tudor et al., 2019) [17].
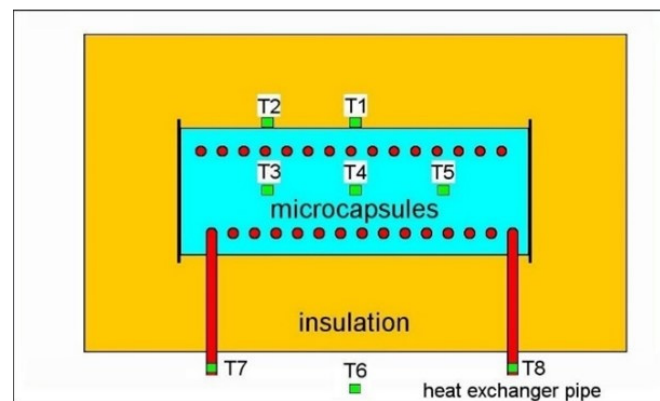
Figure 1. Schematic drawing of the prototype tank (median longitudinal section—viewed from the top): light blue—microcapsules, green—T1 to T8 thermocouples, yellow—insulation, red—heat exchanger. T6 is the room temperature thermocouple.

Tank heating–cooling cycles. Precise amounts of microcapsules were successively loaded into the storage tank (as powder) to total 15.75, 19.232, and 22.067 kg. After each load, the tank was subjected to several charge–self-discharge cycles. A cycle consists of a heating phase, when HTF (360–375 °C) circulates inside the heat exchanger until T1 to T5 readings are all above the melting temperature of sodium nitrate, then it follows the self-discharging phase when the HTF pump is off and the tank is left to cool by itself downward to room temperature.

Adapted calorimetric method. To assess the amount of thermal energy available as latent heat in the storage tank, a heat flow calorimetry method was developed. It is based on temperature monitoring in key points inside and outside the tank, thus estimating the heat loss through the thermal insulation of the tank.

The method considers a quasi-static approximation to Fourier's law:

$$Q/dt = -K\Delta T_{in\text{-}out},$$

with dt as the time interval for measurements, short enough to approximate a constant $\Delta T_{in\text{-}out}$. The approximation is intended to simplify the calculation, as it was determined that the use of differential form to account for $\Delta T_{in\text{-}out}$ changes does not significantly improve the precision for a narrow temperature interval around 300 °C. In the tank setup, at the time-point t, $\Delta T_{in\text{-}out} = tT1 - tT6$, where tT1 and tT6 are the temperatures indicated by T1 and T6, respectively.

For two different material loads of the tank with masses m_1 and m_2, it may be written:

$$Q_{m1}/dt_1 = -K \, \Delta T_{in\text{-}out} \tag{1}$$

$$Q_{m2}/dt_2 = -K \, \Delta T_{in\text{-}out} \tag{2}$$

where K is a proportionality coefficient for heat transfer from the storage tank to the environment. A third equation considers the caloric capacities of the tank components for the two loading m_1 and m_2, resulting in:

$$Q_{m2}\text{-}Q_{m1} = (m_2 - m_1) \, c_p \, dT \tag{3}$$

where dT is a small temperature change that occurred in dt_1, the same that occurred in dt_2 (temperature decay in experimental T1, immediately after the 8–9 h plateau interval—characteristic for latent storage); and c_p is the specific heat of the storage material (microcapsules), determined by DSC just below the solidification offset temperature. For tank calculations, dT is monitored from the T1 curve; the difference between T1 and T2 affects $\Delta T_{in\text{-}out}$ estimation less than 8% in the relevant temperature interval. In the tank experiments, a T1 curve just below solidification (point indicated by the offset temperature in T4) is almost a straight line, therefore the dt (respectively, dT) can be quite large without affecting the integration of heat flows to Q_{m1} and Q_{m2} heats for Equation (3).

Thermal analysis using transient nonlinear FEM.

Model and implementation. The tank model was implemented in Microsoft Excel spreadsheets, with the FEM simulation step progressing on the columns of a simulation table. Visual representation (time course, temperature dependency, etc.) of input parameters and output results was available in charts. To estimate the heat transfer, the tank was modeled as a cylinder, then FEM was applied for 10 concentrical layers (cells), imposing T1 boundary conditions from the experimental dataset. Only conductive transfer was taken into consideration, as suggested by Guo and Zhang (2008) [18] for sodium nitrate. Heat transfer during PCM solidification was calculated by the apparent capacity method, derived from the enthalpy method (Kousksou et al., 2012; Khattari et al., 2020) [19,20]. Thus, microparticle heat transfer during solidification was modeled based on conversion of the solidification heat into specific heat. Thermal conductivity and specific heats were then approximated on specific intervals by polynomial functions on temperature to best fit the experimental data. For a narrow T4 interval at the onset of solidification, a constant thermal conductivity value, 2× higher than measured, was in place for T4 simulations, as it was the single major contributor to simulation–measurement overlap on that interval, probably due to some convective heat transfer by microcapsule deformation in the tank.

Simulations start from the presumed steady-state equilibrium reached at the end of the charging phase. Thus, inside the tank, the radial symmetric temperature distribution was set to range linearly from maximal temperature (T4) to the lowest temperature (T1). After few cycles of initial calculation, the temperature differences between consecutive cycles converged in each calculation point, therefore reaching a more realistic radial temperature distribution than initially assumed. This calculated quasi-steady state was attained with time–space resolution of the FEM mesh (time step 0.25 s and layer thickness 10–2 m) that ensured agreement with the second principle of thermodynamics.

Model limitations and corrections.

Symmetry assumptions. The radial symmetry of the tank is broken on partial tank filling because of the flat horizontal lining at the top of the storage material. In our model, this affects the cross-layer transfer in the material, introducing parallel heat transfer (microcapsule–air in parallel with microcapsule–microcapsule) for a same FEM layer. To overcome this without increasing FEM mesh complexity, for adjacent layers we calculated the effective transfer area (representing only the layers contact within the microcapsule-material block), and use it to express the exchanged heat. Thus, radial heat transfer between consecutive layers occurred on local temperature difference and effective transfer area. Transversal heat transfer occurred for each layer across the insulation, also considering

the effective transfer area and T2–T6 temperature gradient (same for all layers, which is justified by a conductive steel plate that contacted all layers at the side-end). Symmetry across a vertical transversal plane intersecting the tank center was assumed. At each simulation step, the transferred thermal energy was assigned to respective layers, and then a new set of temperatures was calculated.

Experimental temperature readings were shifted from real values by thermocouple shielding. This occurred in the one-end-closed sheath tubes (T3, T4, T5) used to protrude with thermocouples at deep places inside the storage material. Therefore, with the tank empty, we performed a verification experiment for thermocouple readings calibration. A thermocouple was placed at T3 through the protruding tube and another thermocouple, in the same spot, from the inside the tank. The sheath of T3 separated the two thermocouples. The tank was then heated and T3 inside–outside values were recorded. A lag in T3 outside readings was observed. Temperatures were not corrected, as the value is change-rate dependent; instead this temperature difference was acknowledged in the calculations (by the adapted calorimetric method) for the stored energy, and reported distinctively for maximally corrected and uncorrected readings.

Input and output data for simulation: A cycle of FEM simulation consisted in complete calculation of the cell array. For each cell, the cycle output was (a) the amount of energy transferred between the respective cell and the surrounding cells, (b) the end-cycle temperature, and (c) the mass ratio between melt/solid PCM in a cell. Microcapsule experiments (Hot Disk and DSC) provided the thermal conductivity, specific heat, and heat of fusion of the storage material at various temperatures. In FEM, feed-in data for those temperature-dependent thermal parameters were generated by polynomial interpolation (up to grade 6) on multiple segments in the 30 to 380 °C interval. The heat of fusion was expressed as apparent specific heat, to account for the temperature - dependent heat-flow profile in the narrow temperature interval from solidification onset to solidification offset. Simulated T4 temperature evolution was compared with the corresponding experimental values.

3. Results

3.1. Microencapsulation of NaNO₃ Is Persistent in the Storage Tank, over Multiple Thermal Cycles

Our simplified protocol for $NaNO_3$ microencapsulation produced microcapsules 100 to 300 microns in diameter. The microcapsule shell is made of ZnO particles arranged in a nonuniform layer ranging from a few nanometers up to 3 microns thickness. Based on relevant SEM samples, a gross estimation of the whole population of microparticles suggests a majority of well-coated and thermally stable microparticles, with some prone to collapse from thermal cycles. To test their collective thermal stability, the $NaNO_3$–ZnO microcapsules were loaded in the storage tank and exposed to multiple melting–solidification cycles.

Scanning electron microscopy (Figure 2) was employed to demonstrate that microencapsulation was effective and that it is lasting after charge–discharge cycles in the tank. Just after preparation, the microcapsule material was a powder consisting of relatively large (~300 μm) grains. Some of the grains presented a nonuniform gray surface, with light and dark spots (Figure 2A). Figure 2D confirmed that light gray areas are ZnO particles encapsulating $NaNO_3$ grains (dark gray). The correlation was established by EDS (Figure 2C) and grayscale analysis on the small surface spots was pictured in Figure 2E. Thus, elemental concentration (%) of each spot was plotted against the spot intensity on the digital image (grayscale: 0 to 255). On microcapsules that are similar to the microcapsule in the center of Figure 2A, due to the interruptions in the ZnO cover layer, the thickness of the layer can be estimated at the edges of the 2D grain shape. Figure 2B shows the microcapsule-based material after multiple thermal storage cycles in the tank. It compacted into a porous block with microcapsules (smaller than 100 μm) that are often distinctly arising and are bonded by interstitial $NaNO_3$. Whereas before storage cycles some microcapsules were nonuniformly covered with ZnO particles, with areas of exposed $NaNO_3$ core, partially covered microcapsules are absent from material samples after repeated melting–solidification.

(A)

(B)

Element	Weight %	Atomic %	Net Int.
ENERHIGH | NaNO3-ZnO-1 | EDS Spot 2			
C K	49.4	70.18	280.19
O K	20.52	21.88	122.56
ZnL	29.83	7.78	157.79
AlK	0.25	0.16	2.69
ENERHIGH | NaNO3-ZnO-1 | EDS Spot 3			
C K	41.16	66.3	313.97
O K	17.49	21.15	182.14
ZnL	40.64	12.03	358.6
AlK	0.72	0.51	11.7
ENERHIGH | NaNO3-ZnO-1| EDS Spot 4			
C K	18.46	27.95	285.73
N K	11.72	15.21	157.56
O K	36.18	41.12	802.84
ZnL	21.24	5.91	311.68
NaK	12.4	9.81	286.35
ENERHIGH | NaNO3-ZnO-1| EDS Spot 6			
C K	21.74	33.66	308.36
N K	9.72	12.91	111.41
O K	32.21	37.44	663.77
ZnL	25.55	7.27	364.07
NaK	10.78	8.72	234.75

(C)

(D)

(E)

Figure 2. SEM micrograph of $NaNO_3$–ZnO microcapsule before (**A**) and after repeated melting–solidification cycles (**B**). EDS analysis (**C**) of 4 spots in a same picture (**E**), confirming (**D**) that light grey spots contain Zn and do not contain Na or N.

The chemical composition was analyzed on small samples taken from 14 spots at various depths (0 to 45 mm from the front section surface) and radial positions within the storage material. The $NaNO_3$–ZnO mass ratio diminished in most of the spots from an initial value 4:1 to 3.4:1 ($\pm$0.14 standard deviation). Table 1 groups in three intervals the $NaNO_3$:ZnO mass ratio detected in the 14 spots. Most of the microcapsule samples had a mass ratio around 4:1, showing that the chemical composition was preserved locally. For the spots outside the average range, a plausible explanation is that during the liquid phase of the storage cycles, the $NaNO_3$ content of weakly formed microcapsules leaked in the interstitial space and bonded at solidification with stable microcapsules, in a porous material. The ZnO coating of the collapsing microcapsules redistributed to surroundings. Gravitational stratification occurred, proven by composition analysis of six spots from the upper side versus six spots from the lower side of the tank. Thus, average $NaNO_3$–ZnO mass ratios of 3.4 $\pm$ 0.1 at the upper half of the tank and 4.9 $\pm$ 1.6 at the bottom were obtained.

Table 1. Analysis of microparticle composition stability by NaNO$_3$–ZnO mass ratio after multiple phase-change thermal cycles.

NaNO$_3$:ZnO (Mass Ratio)	3.4:1 ÷ 4:1	4:1 ÷ 8:1	above 60:1
Count (no. of spots)	9	3	2

3.2. Temperature-Dependent Thermal Properties of NaNO$_3$–ZnO Microcapsules

Latent heats of NaNO$_3$ solid–liquid transitions were determined by DSC experiments in microcapsules and pure salt (Figure 3). For microcapsules, the melting heat was 102.564 kJ/kg and the solidification heat was 94.5 kJ/kg. In addition, the specific heat at 284.8 °C was 0.824 kJ/kg. Pure NaNO$_3$ required 124.5 kJ/kg for solidification. For microcapsules, the temperature intervals for melting and solidification are [t_{onset}, t_{offset}] = [303, 319] °C and [302.5, 285] °C, respectively (Figure 3A). This does not significantly differ from pure salt, (Figure 3B—our data). Thus, in the DSC experiments at 10 °C/min cooling rate, supercooling tends to be less pronounced in microcapsules, and clearly reduced compared with similar experiments on pure NaNO$_3$, as reported by Mohammad in his Ph.D. thesis, Table 7.2.2.1. [5]. The higher solidification heat (modulus) reported there (167 kJ/kg) for NaNO$_3$ is partly related to the fact that our measurements were done for repeated melting–solidification cycles, with latent heat in the first-cycle consistently higher than the rest; converging to the reported value). The onset and offset temperatures (solidification) were used in simulations and in calorimetric calculations. In FEM simulations, the normalized DSC curve profile and solidification latent heat were principal determinants of the T4 temperature evolution, whereas calorimetric calculations used onset and offset temperatures from DSC to precisely identify the interval for latent heat contribution to the experimental T4 curve.

(A)

(B)
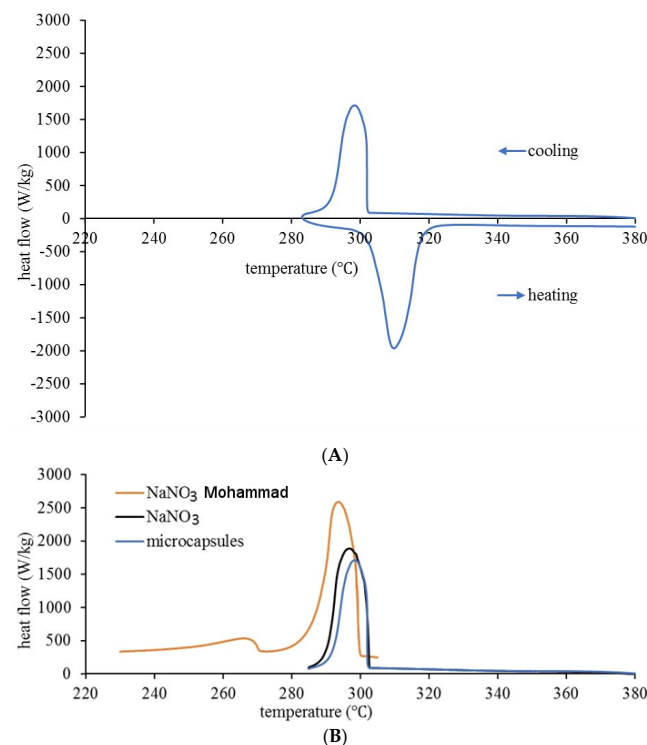
Figure 3. (**A**) DSC heating - cooling curves for NaNO$_3$–ZnO microcapsules. (**B**) Comparison of DSC solidification curves (10 °C /min cooling rate) for pure NaNO$_3$ (Mohammad [5] and own data) and microcapsules.

Figure 4 presents the specific heat and the thermal conductivity of microcapsules in comparison with pure NaNO$_3$ (own experiment and from Bauer et al., 2013 [21]). In the

temperature interval from 303 to 285 °C the Hot Disk values are not shown (data from DSC were used in calculations). In the temperature interval 30–270 °C, the thermal conductivity of the microcapsules is around 0.3 W/m·K. At 280 °C, a minor decrease in thermal conductivity was noticed, probably associated with phase transition for $NaNO_3$ crystalline structure. Above 300 °C, a sudden increase in the thermal conductivity was measured, correlating with PCM melting. The room temperature density of the microcapsule-based storage material after several melting–solidification cycles was calculated, considering the density decrease when increasing temperature, as reported for $NaNO_3$ [21]. A value of 1.8 t/m^3 was inferred and used for FEM simulations (at temperatures just below the liquid–solid transition temperature).
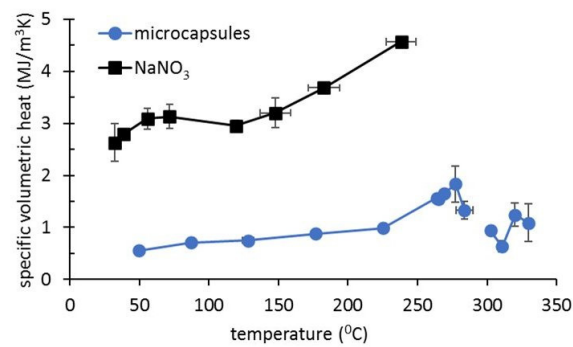
(**A**)
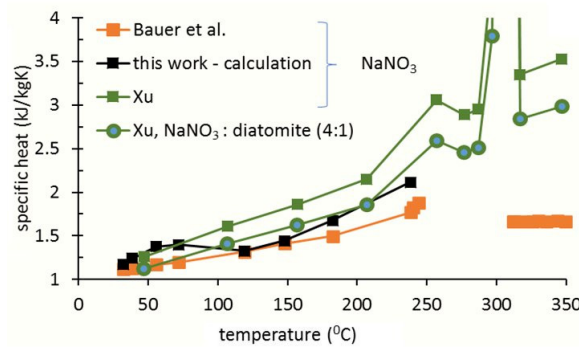
(**B**)
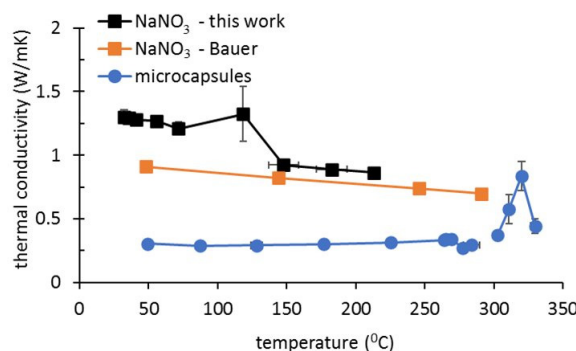
(**C**)

Figure 4. Thermal properties of $NaNO_3$–ZnO microcapsules in comparison with pure $NaNO_3$. Hot Disk determinations (own data) of volumetric specific heat (**A**) and thermal conductivity (**C**), in comparison with other works. (**B**) Specific heat of pure sodium nitrate and of a composite mixture of $NaNO_3$: diatomite (same weight ratio as microcapsules). External data are from Bauer et al., 2013 [21] and Xu et al., 2017 [4].

3.3. Availability of High-Temperature Thermal Energy from Microcapsule Storage

In a typical charge–self-discharge experiment (Figure 5) the highest temperatures are almost always recorded by T4, in the center of the tank, near the heating coil. T1 is placed on the surface of the stainless-steel shell, on the same transversal section as T4, and therefore used in conjunction with T4 to monitor the temperature in radial direction across the storage material. The presumed left–right symmetry from the center of the tank is consistent with T3 versus T5 readings.
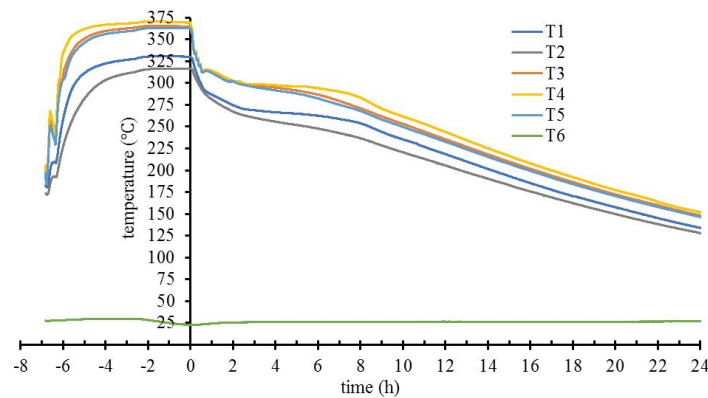
Figure 5. T1 to T6 temperatures readings (positions in the prototype tank indicated in Figure 1) during a heating–cooling cycle.

In Figure 6, plateaus of relatively constant T4 and T1 temperatures are noted shortly after the beginning of the free-cooling phase of cycles. For T4, this corresponds to the liquid to solid phase transition when latent energy is released from microparticle cores at rates that dominate over sensitive heat. After PCM solidification phase, the temperature decay in tank is controlled by two variables: the caloric capacity of the tank and the heat transfer through tank insulation. For a narrow temperature interval, using linear fit slopes of T1 curves corresponding to 19.23 and 22.07 kg (taken near the PCM offset temperature), K value was determined. Based on the T1 plateau, by extrapolating a constant K towards t = 0 h, the heat transfer rate was calculated, thus estimating the latent PCM energy stored in the tank.

(A)
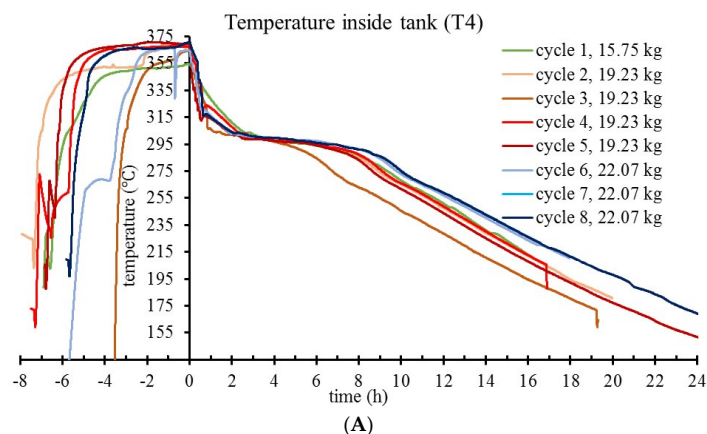
Figure 6. *Cont.*
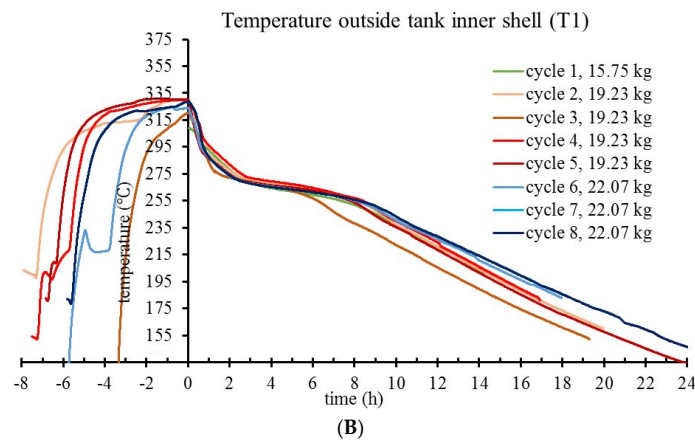
Figure 6. T4 (**A**) and T1 (**B**) temperature evolution during charge–self-discharge cycles of the prototype tank, for progressively increased loads of storage material.

In the evaluation of the thermal energy storage capacity of the tank, two loads of microcapsules were considered: 19.23 and 22.07 kg. T4 monitors the solidification in the innermost spot of the tank, therefore informative for the end of the latent heat release phase. At high temperature change rates, T4 readings are affected by nonequilibrium, with measured temperature differences up to 15 °C for the interval of interest. Thus, to protrude with the T3–T5 thermocouples at their deep spots into the storage material, the tank has three thin tubes welded on the longitudinal side. The tubes are closed at the protruding end and they prevent direct contact between thermocouples and microcapsules. In an experiment to determine the magnitude of correction, another thermocouple was inserted into the air-filled storage tank, with the tip measuring the temperature in the same spot as T4, but from inside the tank. In the experiment presented in Figure 7, for T_{real} = 275 °C, the $T_{measured}$ is 260 °C - showing up to 15 °C temperature differences. This is explained by nonequilibrium measurements for T3 - T5 during tank heating. Correction of T4 on this basis is not straightforward, since at plateau temperature (in the solidification phase) the temperature equilibrium between material and sensor is attained. Therefore, a correction was not applied to thermocouple readings. Instead, in Figure 8, when reporting the energy available as latent heat (by adapted calorimetric method) in tank discharge, a 15 °C uncertainty on T4 readings was explicitly acknowledged for the solidification offset temperature, and the corresponding energy values given as a maximum estimate.
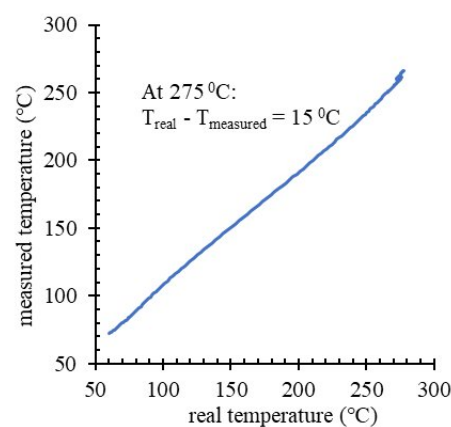
Figure 7. The accuracy of T3–T5 thermocouple response to temperature dynamics inside the storage tank.
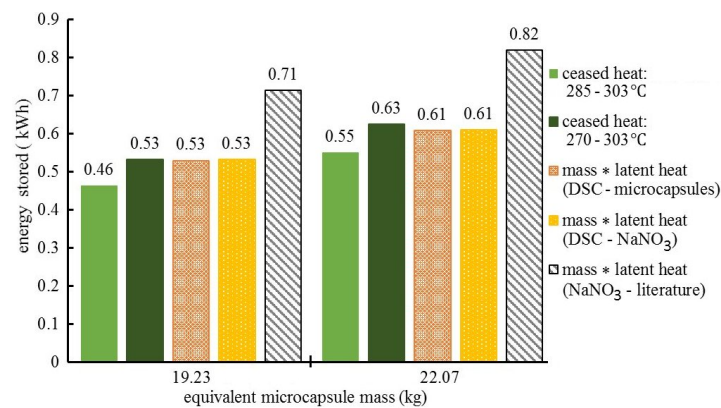
Figure 8. Storage tank evaluation of the latent heat thermal energy storage in microcapsules by adapted calorimetric method (ceased heat) and latent heat measurements at microscale.

Based on the latent heats, a summary is provided in Figure 8 for the estimates of the energy stored as latent heat in the partially filled storage tank. Results are presented for microcapsules in comparison with pure $NaNO_3$ at equal PCM content mass. Two tank loads were considered: 19.23 and 22.07 kg of microcapsules, with a net $NaNO_3$ content of 15.38 and 17.65 kg, respectively. In the calorimetric method adapted, the phase-change-stored thermal energy is the heat ceased by the tank in the temperature interval for solidification, with T4 as the monitor. Solidification in microcapsules was considered for uncorrected [285, 303] °C and maximally corrected [270, 303] °C temperature intervals. A specific heat of 0.824 kJ/ kg resulted from DSC measurements and it was used to implement Equation (3). The first two columns at each tank load represent the estimations of the stored energy by this adapted calorimetric method. The ceased heat is compared with tank-level calculations based on (a) microscale DSC measurements of the latent (solidification) heat for microcapsules and $NaNO_3$, and (b) the reference (literature) latent heat (167 kJ/kg) for $NaNO_3$.

The columns labeled as mass * latent heat represent estimates of the tank-stored PCM solidification energy, and are provided by the mass–latent heat product for microcapsules (DSC) and pure $NaNO_3$ (our DSC and literature). The mass of pure $NaNO_3$ corresponds to the PCM content of microcapsules.

3.4. Tank Discharge Insight View by FEM Simulation

In our FEM model tank, for 19.23 and 23.06 kg microcapsules loads, the discharge phase (of the experimental charge–self-discharge cycles) was simulated. T1 and T2 readings from real experiments were the boundary temperatures for tank inner shell: T1 on longitudinal and T2 on transversal margins. The thermal properties of the storage material were kept identical for the two load conditions, with respect to their temperature dependency. The thermal energy transferred at each simulation step was calculated, resulting in the temperature evolution for each layer. T4 experimental readings were compared with corresponding temperatures in simulations. Experimental T1 was imposed in simulations as the temperature of the outer (tenth) layer to predict temperatures at each of the nine inner concentric layers. T2–T6 was used for all layers as the temperature gradient on the lateral side of the tank. In Figure 9, a good fit between experimental and simulated T4 curves indicate that the model and parameters are accurate, thus validating thermal conductivities, specific heats, and solidification heat data. The main parameter controlling the overlap between simulated and experimental T4 in the plateau area was the latent heat of liquid–solid transition. The specific heat of microcapsules provided the slope of the T4 curve below solidification offset temperature. At the beginning of the discharge phase, the fast T4 decay could only be reproduced in simulations with thermal conductivity >200% of the Hot Disk value. Various factors contribute to this unfitted section of the T4 decay,

among which may be considered T4 thermocouple shielding and convective heat transfer via gravitational leakage of low viscosity interstitial (nonencapsulated) PCM.
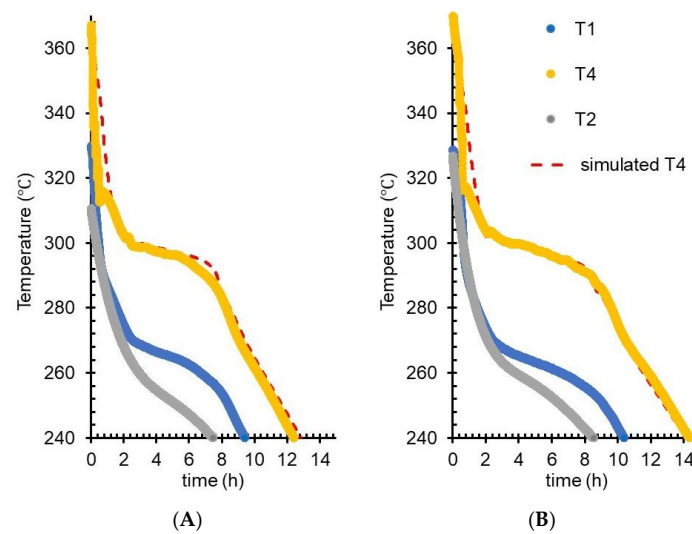
Figure 9. FEM simulations of T4 (red segmented line) in the self-discharge experiment, compared with experimental data (filled circles) for T1 (blue), T2 (gray), and T4 (yellow): (**A**) 19.23 kg microcapsules load and (**B**): 22.07 kg load.

4. Discussion

PCM microencapsulation aims to enhance the properties of materials for thermal energy storage and holds potential to provide effective solutions for applications in heating systems (Huang 2019) [8]. Microencapsulation of $NaNO_3$ in ZnO shell for high temperature thermal energy storage may reduce the investment cost of using high-grade stainless steel (Fernandez et al., 2014) [22] to contain the highly corrosive salt (Tudor et al., 2018) [16]. In Tudor et al., 2018 [16], a solvothermal process was used to produce nanometer-thick zinc oxide shells around potassium nitrate cores, obtaining microcapsules of few microns size. In the present paper, preparation of larger size (100 to 300 μm) microparticles is reported, each encapsulated in a layer of ZnO nanoparticles. Due to changes in the microencapsulation protocol (solvothermal synthesis was eliminated), the ZnO envelopes reported here typically show highly variable thickness, ranging from few nanometers to few microns.

Initially uneven, the shell ZnO layer of microcapsules seems to uniformly distribute upon melting–solidification, and thus resists multiple charging–discharging cycles. In this view of a potential for improvements in ZnO deposition, a 4:1 $NaNO_3$: ZnO mass ratio may be lower than optimal, where optimization means that for complete covering of the microparticle, the ratio should maximize the PCM mass on the expense of shell thickness. Despite this suboptimal PCM:shell ratio, our novel simplified protocol for microencapsulation may minimize the initial investments in specialized equipment for manufacturing. The observed thermal stability of microcapsules reported here may be explained by the fact that melting–solidification of PCM is able to select, after few cycles, structurally stable microcapsules. With the leaking PCM, compaction of the storage material at macroscale may occur, increasing the thermal energy density in storage cycles.

The temperature dependency for density, thermal conductivity, and specific heat of pure $NaNO_3$ is available from multiple sources (Xu et al., 2018; D'Aguanno et al., 2018; Bauer et al., 2017) [4,6,21]. Therefore, it was possible to compare our data (Figure 4B) in the same graph with results reported by Xu et al., 2018 [4] for $NaNO_3$ and for a mixture of diatomite: $NaNO_3$ at the same weight ratio as our $NaNO_3$:ZnO (4:1).

From Figure 4A, which shows the volumetric specific heat, it is possible to calculate the specific heat (gravimetric) of the material by considering the temperature dependency of the material density. Since the density for the microcapsule-based material was not

measured for high temperatures, a temperature variation similar to that described for NaNO$_3$ [21] was assumed. In the temperature interval from 50 to 284 °C, a value between 300 and 1020 J/kg·K resulted from the calculations of the specific heat of microcapsules; particularly important at 284 °C, where the specific heat for microcapsules is 801 J/kg·K. FEM simulations (Figure 9) validated 750 J/kg·K as the only value of the specific heat that allows consistent overlap below the solidification T$_{offset}$ with the experimental T4 slope (for both tank loads). For Equation (3) in the adapted calorimetric method, the 824 J/kg·K value (measured by DSC) was used; this is near 801 J/kg·K value deduced from volumetric specific heat, and close to the 750 J/kg·K value from FEM validation. Thus, FEM simulations not only reproduce the experimental temperatures, but are useful to estimate the accuracy of other methods (e.g., DSC and adapted calorimetric method) by selecting, from multiple fitting (simulation) sessions, a specific set of values for the material thermal parameters.

Multiple applications are designed to simulate thermal transfer (Al-abidi et al., 2013) [11]. While designing a standalone CFD application [17] capable of reproducing complex geometries, it was observed that a simplified cylinder model of the storage tank is sufficiently informative and fast to produce end-simulation results. The FEM simulations require as input the (a) tank geometry, (b) thermal properties of the storage material (from laboratory measurements), and (c) time course of temperature on the tank shell (monitored in tank charge–discharge experiments). The simulation output is a time course for temperatures and thermal energy distribution in the virtual tank, confirmed by thermocouple temperature monitoring in the center of the prototype storage tank.

The FEM model allows to evaluate to which degree accuracy is needed for thermal property inputs (thermal conductivity and specific heat), and whereas polynomial fits are good descriptors for experimental data. The unusual choice of Microsoft Excel for the implementation of FEM simulations is based on the cylindrical symmetry and the simplicity of the storage tank, allowing for massive reduction in the mesh size. The validity of the simplification was tested by the convergence of the result, in each cell, for an interval of time steps ranging from 0.1 to 0.5 s. Although in terms of computing resources needed at a glance, Excel simulation approach is more demanding than an equivalent runtime simulation application, it has the advantage of facilitating development of features such as graphically augmented, transparent, and explicative input and output data (Tomimura et al., 2009) [23].

The main question to which this study responded is if high temperature thermal energy may effectively be recovered from storage in microcapsules. In a simplistic evaluation of the tank-stored latent energy, the latent heat of microcapsules is multiplied by their mass, providing a target value (maximal) for the potential of the tank. In real thermal storage cycles, a PCM material is not uniformly exposed to energy transfer during tank charging; melting of all available PCM mass depends on factors such as thermal conductivity of the microcapsules, charging time, and temperature in the heat exchanger circuit. This is evident in the charge–self-discharge cycle 3 (Figure 6), when a plateau temperature (quasi-steady state) was not reached at charging time, therefore the high-temperature discharge phase was shorter. Ideally, when charging is complete and all NaNO$_3$ content is liquid, most of its latent heat is retrievable at temperatures that correspond to latent heat storage.

Figure 8 presents the high temperature energy that can be retrieved from NaNO$_3$–ZnO microcapsules, which corresponds to specific energy storage of 80.5 kJ/kg as the low estimate and 99.5 kJ/kg as the high estimate. These values are comparable with specific energies for other inorganic salt-based PCMs [24,25]. The corresponding energy density range (1.45 × 105 to 1.79 × 105 kJ/m^3), considering 1800 kg/m^3 for the microcapsule material density (after melting–solidification cycles), is also as expected.

Noticeable differences of the NaNO$_3$ tank-stored energy exist (Figure 8) when calculations are based on literature data versus this work's DSC measurements. This is explained by a drop of the NaNO$_3$ latent heat after the first melting–cooling cycle, probably due to partial nitrate decomposition (Bauer et. al 2013) [21].

Estimations of the specific energy incorporate several sources of error: (a) the lag in T3–T5 temperature readings presented in Figure 7, (b) small (unintended) variations of experimental conditions in the tank setup (even small sudden changes in the ambient light were spotted in temperature traces), and (c) the precision of the thermocouples that were linearly calibrated for a large temperature interval. Instead of presenting data means from multiple cycles (with error bars), the graphs in Figure 6 show temperature evolutions for each cycle, which is more informative for tendencies that fall under statistical thresholds. With four cycles on 19.23 kg load and three cycles on 22.07 kg load, data show no pattern for temperature–trace variation between cycles of a same load, whereas temperature traces corresponding to different loads are clustered. By reporting a range for the estimated specific energy density of microcapsules (from Figure 8 data) instead of a data mean and error bars, this work acknowledges limitations in the precision of the adapted calorimetric method to measure the latent heat that is stored in the prototype tank. Nevertheless, alternative methods such as heat flow balance focused on monitoring the difference between T8 and T7 during active HTF pumping/extraction are seriously affected by the thermocouple precision (± 1.5 °C) and the possibility to monitor HTF flow rate, while still dependent on estimation of heat flow through tank insulation.

The workflow for design research and development of a new solution for latent heat energy storage was charted by Whiffen and Riffat (2013) in their Figure 5 [24]. It comprises several parallel activities already reported for the ENERHIGH project [13,15–17], such as selection of materials in the appropriate range, design, and development of the heat exchanger and construction of the prototype. Here, laboratory measurements of microcapsule thermophysical properties and prototype experimentation converge to FEM simulation, in a platform for integrated material design and testing, to be used for enhancement of relevant properties and optimization of material use in product applications.

To better evidence the process and optimize charging/extraction for intermittent energy sources, FEM simulations with adequate geometry details can produce time-resolved 3D maps of heat transfer and the possibility to explore various real-use scenarios. Work is in progress to design and implement a software application that enables FEM simulations for complex geometries of the storage tank and spatial resolutions of only a few millimeters (Tudor et al., 2019) [17]. Implementing methodological solutions from the current study, a simulation application may be able to reproduce thermal transfers with higher fidelity during melting–solidification. The nonlinear temperature dependencies of thermodynamic parameters (thermal conductivity and apparent specific heat) may be obtained from laboratory determinations and used as input in FEM simulations to produce overlap with the experimental temperature curves; the outcome is exemplified in Figure 9.

5. Conclusions

This work presents laboratory and prototype-scale characterization of an innovative PCM for thermal energy storage: (i) thermal properties of $NaNO_3$–ZnO microcapsules; (ii) a prototype tank demonstration of phase-change thermal energy storage; and (iii) a methodological framework for design, scaled manufacturing, and prototype testing of microencapsulated $NaNO_3$. Methodological novelties are: (a) effective manufacturing of microcapsules, (b) a method to measure the high temperature thermal energy stored in a prototype tank, and (c) a software tool (as a document template) to analyze and predict the dynamics of PCM energy storage during charge–discharge cycles of a cylindrical storage tank.

In summary:

- $NaNO_3$–ZnO microcapsules were prepared by a simple and easy to scale protocol, then characterized for structural and thermal properties;
- Charge–discharge experiments of the storage tank demonstrated the availability of high-temperature thermal energy stored as latent heat in $NaNO_3$–ZnO microcapsules;
- The temperature interval to access this energy in the pilot tank is 303 to 285 °C, as predicted by DSC experiments at microscale;

- By the adapted calorimetric method, we estimated that in-tank high temperature specific energy of microcapsules is in the range 80.5–99.5 kJ/kg, in line with expectations for inorganic salts;
- Thermal transfer simulations using the Microsoft Excel template setup for transient nonlinear FEM confirmed that prototype-scale thermal energy storage in microcapsules can be predicted from laboratory measurements on small material samples.

Future work may use the simulation–prototyping platform to develop microencapsulated phase change materials with enhanced thermal conductivity, ensuring optimal heat transfer rates for specific applications.

References

1. Sarbu, I.; Sebarchievici, C. A Comprehensive Review of Thermal Energy Storage. *Sustainability* **2018**, *10*, 191. [CrossRef]
2. Podara, C.V.; Kartsonakis, I.A.; Charitidis, C.A. Towards Phase Change Materials for Thermal Energy Storage: Classification, Improvements and Applications in the Building Sector. *Appl. Sci.* **2021**, *11*, 1490. [CrossRef]
3. Jouhara, H.; Żabnieńska-Góra, A.; Khordehgah, N.; Ahmad, D.; Lipinski, T. Latent thermal energy storage technologies and applications: A review. *Int. J. Thermofluids* **2020**, *5*, 100039. [CrossRef]
4. Xu, G.; Leng, G.; Yang, C.; Qin, Y.; Wu, Y.; Chen, H.; Cong, L.; Ding, Y. Sodium nitrate—Diatomite composite materials for thermal energy storage. *Sol. Energy* **2017**, *146*, 494–502. [CrossRef]
5. Mohammad, M.B. High Temperature Properties of Molten Nitrate Salts for Solar Thermal Energy Storage Application. Ph.D. Thesis, Swinburne University of Technology, Melbourne, Australia, 2016. Available online: http://hdl.handle.net/1959.3/425444 (accessed on 30 June 2021).
6. D'Aguanno, B.; Karthik, M.; Grace, A.N.; Floris, A. Thermostatic properties of nitrate molten salts and their solar and eutectic mixtures. *Sci. Rep.* **2018**, *8*, 1–15. [CrossRef] [PubMed]
7. Bellan, S.; Alam, T.E.; Gonzalez-Aguilar, J.; Romero, M.; Rahman, M.M.; Goswami, D.Y.; Stefanakos, E.K. Numerical and experimental studies on heat transfer characteristics of thermal energy storage system packed with molten salt PCM capsules. *Appl. Therm. Eng.* **2015**, *90*, 970–979. [CrossRef]
8. Huang, X.; Zhu, C.; Lin, Y.; Fang, G. Thermal properties and applications of microencapsulated PCM for thermal energy storage: A review. *Appl. Therm. Eng.* **2019**, *147*, 841–855. [CrossRef]
9. Cáceres, G.; Fullenkamp, K.; Montané, M.; Naplocha, K.; Dmitruk, A. Encapsulated Nitrates Phase Change Material Selection for Use as Thermal Storage and Heat Transfer Materials at High Temperature in Concentrated Solar Power Plants. *Energies* **2017**, *10*, 1318. [CrossRef]
10. Courbon, E.; D'Ans, P.; Skrylnyk, O.; Frère, M. New prominent lithium bromide-based composites for thermal energy storage. *J. Energy Storage* **2020**, *32*, 101699. [CrossRef]
11. Al-Abidi, A.A.; Bin Mat, S.; Sopian, K.; Sulaiman, M.; Mohammad, A.T. CFD applications for latent heat thermal energy storage: A review. *Renew. Sustain. Energy Rev.* **2013**, *20*, 353–363. [CrossRef]
12. Zhang, H.; Balram, A.; Tiznobaik, H.; Shin, D.; Santhanagopalan, S. Microencapsulation of molten salt in stable silica shell via a water-limited sol-gel process for high temperature thermal energy storage. *Appl. Therm. Eng.* **2018**, *136*, 268–274. [CrossRef]
13. Romero-Sánchez, M.D.; Piticescu, R.-R.; Motoc, A.M.; Arán-Ais, F.; Tudor, A.I. Green chemistry solutions for sol–gel microencapsulation of phase change materials for high-temperature thermal energy storage. *Manuf. Rev.* **2018**, *5*, 8. [CrossRef]
14. Lee, J.; Jo, B. Surfactant-free microencapsulation of sodium nitrate for high temperature thermal energy storage. *Mater. Lett.* **2020**, *268*, 127576. [CrossRef]

15. Romero-Sanchez, M.D.; Piticescu, R.R.; Motoc, A.M.; Popescu, M.; Tudor, A.I. Preparation of microencapsulated KNO₃ by solvothermal technology for thermal energy storage. *J. Therm. Anal. Calorim.* **2019**, *138*, 1979–1986. [CrossRef]

16. Tudor, A.I.; Motoc, A.M.; Ciobota, C.F.; Ciobota, D.N.; Piticescu, R.R.; Romero-Sánchez, M.D. Solvothermal method as a green chemistry solution for micro-encapsulation of phase change materials for high temperature thermal energy storage. *Manuf. Rev.* **2018**, *5*, 4. [CrossRef]

17. Tudor, A.I.; Neagoe, C.; Piticescu, R.-R.; Romero-Sanchez, M.D. Microencapsulated PCMs for thermal energy storage in the range 300–500 °C: Pilot-testing. *IOP Conf. Ser. Mater. Sci. Eng.* **2019**, *572*, 012066. [CrossRef]

18. Guo, C.; Zhang, W. Numerical simulation and parametric study on new type of high temperature latent heat thermal energy storage system. *Energy Convers. Manag.* **2008**, *49*, 919–927. [CrossRef]

19. Kousksou, T.; Jamil, A.; El Omari, K.; Zeraouli, Y.; Le Guer, Y. Effect of heating rate and sample geometry on the apparent specific heat capacity: DSC applications. *Thermochim. Acta* **2011**, *519*, 59–64. [CrossRef]

20. Khattari, Y.; El Rhafiki, T.; Choab, N.; Kousksou, T.; Alaphilippe, M.; Zeraouli, Y. Apparent heat capacity method to investigate heat transfer in a composite phase change material. *J. Energy Storage* **2020**, *28*, 101239. [CrossRef]

21. Bauer, T.; Pfleger, N.; Laing, D.; Steinmann, W.-D.; Eck, M.; Kaesche, S. 20-High-Temperature Molten Salts for Solar Power Application. In *Molten Salts Chemistry: From Lab To Applications*; Lantelme, F., Groult, H., Eds.; Elsevier: Oxford, UK, 2013; pp. 415–438. [CrossRef]

22. Fernández, A.G.; Galleguillos, H.; Pérez, F.J. Thermal influence in corrosion properties of Chilean solar nitrates. *Sol. Energy* **2014**, *109*, 125–134. [CrossRef]

23. Tomimura, T.; Koito, Y.; Torii, S.; Ishizuka, M. Application of Excel to Thermal Analysis of Electronic Equipment: Program-Less Analysis and Visualization of Its Process by Using Spreadsheet of Excel. In Proceedings of the ASME 2009 InterPACK Conference, San Francisco, CA, USA, 19–23 July 2009; Volume 2, pp. 527–533. [CrossRef]

24. Whiffen, T.R.; Riffat, S.B. A review of PCM technology for thermal energy storage in the built environment: Part I. *Int. J. Low Carbon Technol.* **2012**, *8*, 147–158. [CrossRef]

25. Dincer, I.; Rosen, M.A. Energy Storage Systems. In *Thermal Energy Storage Systems and Applications*, 2nd ed.; Wiley & Sons: Chichester, UK, 2011; pp. 57–92.